PAPER

Check for updates

Asymmetric microfiber actuators with reciprocal deformation†

Yuhang Lu, [iD] ‡[a] Shiyu Wang [iD] ‡[a] and Pingan Zhu [iD] *[ab]

With the trend towards miniaturization in soft robotics, most microactuators encounter challenges in achieving versatile deformations. Here, we present an innovative microactuator design featuring reciprocal deformation, activated solely by humidity changes. These microactuators adopt an asymmetric microfiber configuration, characterized by a core–shell structure with a hydrophilic shell encapsulating hydrophobic microparticles. Utilizing droplet microfluidics for fabrication enables precise control over microfiber morphology and internal microparticles. During hygroscopic actuation, these microactuators undergo a unique two-stage deformation, exhibiting opposite trends in curvature variation—a stark departure from the unidirectional deformations observed in previous microactuators. The anisotropy inherent in asymmetric microfibers governs water absorption and desorption, driving this distinctive reciprocal deformation. These microactuators demonstrate versatility in controlled droplet transport and solid cargo manipulation, expanding their potential applications. This study not only unveils novel mechanisms but also broadens the functional spectrum of microactuators.

1 Introduction

In the development of robotics, a prevailing trend centers around the miniaturization of robotic components, driving innovations in microactuators. These microscopic devices have garnered considerable research attention and exhibit substantial promise across diverse domains such as micro-lifters,[1] micro-joints,[2] artificial muscles,[3–5] energy harvesting,[6] biomedicine,[7–10] microvalves,[11] liquid seals,[12] bioinspired transparency,[13,14] color change,[15] and beyond. To power and maneuver these microactuators, a spectrum of energy sources has been harnessed, including light,[16–20] electricity,[19,21–23] acoustics,[24] thermal energy,[18] magnetic fields,[25–27] and chemical reactions[28,29] (Table S1, ESI†). The choice of materials for microactuators spans composites,[26,30,31] carbon nanotubes,[22,30] liquid crystal elastomers,[5,32–34] and biodegradable[35,36] and hygroscopic[36] polymers[20] and more. The evolution of microactuators propels the advancement of microrobots, contributing to the ongoing evolution of

technology towards miniaturization and facilitating exploration at the micrometer and even nanometer scales.

While existing microactuators demonstrate remarkable capabilities, the majority are confined to unidirectional deformation, posing limitations in scenarios demanding multiple deformations. The need for multiple and intricate deformations is particularly pronounced in practical applications, where conventional microactuators fall short. For instance, the ability to execute complex deformations can liberate microactuators from constraints, such as being limited to transporting items to a target area and lacking the capacity to autonomously retreat from the target location post-task completion. The capacity to move away from the target location post-transportation can mitigate the impact of microactuators on the target site and enhance task efficiency through cyclic and recyclable transportation.

Alternatively, some existing microactuators rely on multiple energy sources to sustain complex deformations and revert the actuator to its original state. This reliance on multiple energy sources introduces limitations, especially in scenarios where such energy sources are either unavailable or inaccessible. Achieving complex deformation in microactuators using a singular energy source remains a great challenge.

To address these limitations, we introduce an innovative design of soft microactuators capable of intricate deformations solely in response to humidity changes. These

[a] Department of Mechanical Engineering, City University of Hong Kong, Hong Kong, China. E-mail: pingazhu@cityu.edu.hk

[b] Shenzhen Research Institute, City University of Hong Kong, Shenzhen, China

† Electronic supplementary information (ESI) available: Table S1, Fig. S1 and S2, and Movies S1–S5. See DOI: https://doi.org/10.1039/d4im00017j

‡ These two authors contribute equally to this work.

© 2024 The Author(s). Co-published by the Institute of Process Engineering, Chinese Academy of Sciences and the Royal Society of Chemistry

Ind. Chem. Mater., 2024, **2**, 441–450 | **441**

soft microactuators take the form of asymmetric microfibers, featuring a core–shell structure manufactured through droplet microfluidics technology. Through hydration (or dehydration), these asymmetric microfiber actuators undergo a unique two-stage deformation where the radius of curvature first decreases (or increases) and then increases (or decreases). This starkly contrasts with the conventional unidirectional deformation of microactuators, where the radius of curvature monotonically increases or decreases during actuation. This distinctive actuation is termed "reciprocal deformation", a behavior attributed to the anisotropy of the microfiber actuator which regulates the absorption and desorption of water.

The reciprocal-deformation capability observed in these microactuators unfolds new possibilities for controlled droplet and solid cargo transport onto substrates, showcasing their potential applications that transcend traditional actuators limited to unidirectional deformation. This study not only underscores the significant departure from conventional microactuators but also heralds a new era in the development of highly versatile and adaptive microactuation technologies.

2 Results and discussion

2.1 Design principle

Fig. 1 provides a schematic comparison between the unidirectional deformation observed in conventional double-layer actuators (Fig. 1a) and the reciprocal deformation of the designed asymmetric microfiber actuators (Fig. 1b). The disparate coefficients of expansion inherent in the materials of conventional double-layer actuators result in a unidirectional bending deformation, where the radius of curvature decreases monotonically from the initial state 1 to the final state 2 (Fig. 1a). In contrast, Fig. 1b depicts asymmetric microfiber actuators designed to exhibit reciprocal deformation, wherein the radius of curvature undergoes an initial increase (or decrease) followed by a subsequent decrease (or increase) by actuation.

The engineered microfiber is predominantly composed of a composite alginate–diatomite shell encapsulating a ribbon of asymmetric polydimethylsiloxane (PDMS) microparticles positioned eccentrically in proximity to one side of the fiber body. Notably, the alginate–diatomite shell is hydrophilic, while the PDMS cores are hydrophobic (Fig. S1, ESI†). This property contrast allows the shell to modulate its volume in response to changes in humidity, while the PDMS cores remain unresponsive to moisture (Fig. S2, ESI†).

The dynamic processes of hydration and dehydration manifest in four distinct states: state 1 signifies complete hydration, with the alginate–diatomite shell attaining its maximum volume, while state 3 represents complete dehydration, characterized by the smallest volume of the alginate–diatomite shell. State 2 denotes the transitional phase from state 1 to state 3 during dehydration, and state 4 represents the transitional phase from state 3 to state 1 during hydration. Initiating dehydration from state 1 progresses through state 2, marked by an initial increase in the radius of curvature, and culminates in state 3, characterized by a subsequent decrease in the radius of curvature. Throughout this dehydration process, the volume of the microfiber shell progressively reduces. The transition from state 3 to state 1 delineates the water absorption process of the microfiber, with its shell volume gradually increasing. In a fully dehydrated state 3, the microfiber first absorbs water to achieve state 4, wherein the radius of curvature decreases, and subsequently fully absorbs water to revert to state 1, with the radius of curvature increasing.

2.2 Microfluidics-enabled manufacturing

Droplet microfluidic technology was employed in the fabrication of the designed asymmetric microfiber actuators, utilizing core–shell liquid jets as templates (Fig. 2a).[31,37,38] A co-flow microfluidic device was instrumental in this process. The external phase liquid comprised an aqueous mixture of sodium alginate and diatomite, while the internal phase liquid consisted of a blend of PDMS and silicone oil. The
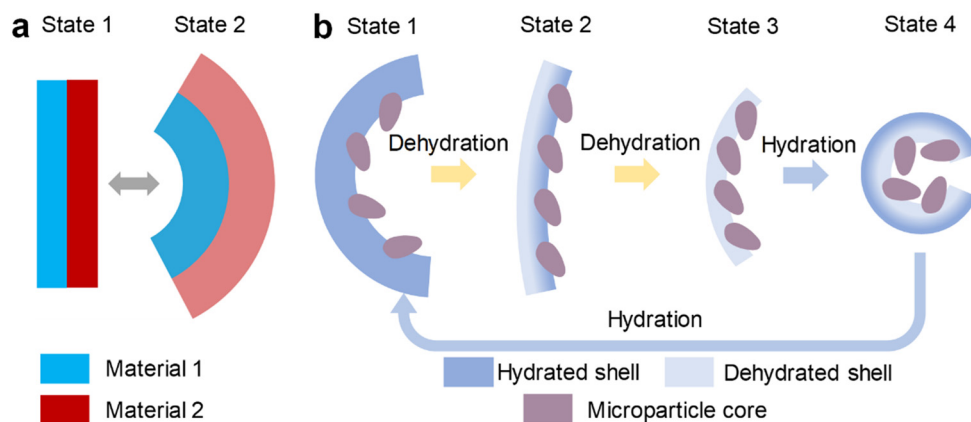

Fig. 1 Schematics illustrating (a) a conventional double-layer actuator with unidirectional deformation and (b) an asymmetric microfiber actuator capable of reciprocal deformation.
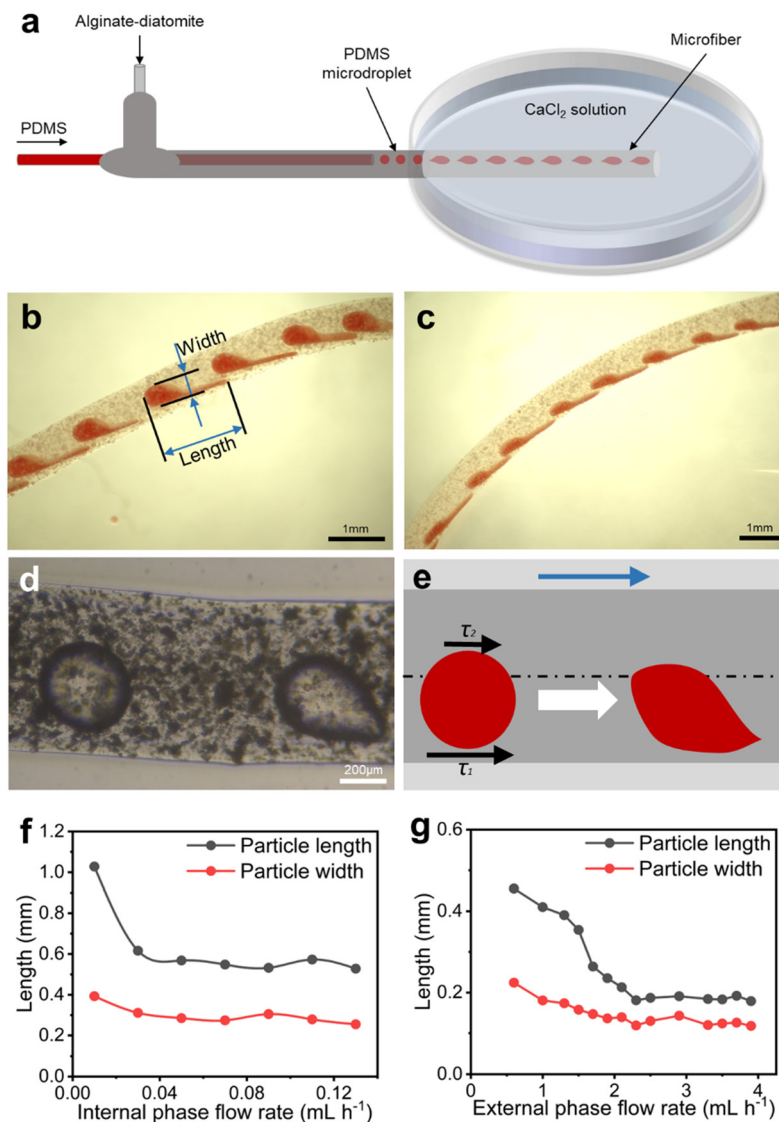
Fig. 2 Microfluidics-enabled generation of the designed asymmetric microfiber actuators. (a) Schematic of the microfluidic device for the fabrication of the asymmetric core–shell microfibers; (b and c) optical micrographs (OM) depicting the manufactured asymmetric microfibers under (b) external flow rate of 2 mL h^{-1} and internal flow rate of 0.7 mL h^{-1}, and (c) external flow rate of 4 mL h^{-1} and internal flow rate of 0.13 mL h^{-1}; (d and e) the OM (d) and schematic (e) representation of the forming microfiber upon contact with CaCl$_2$ solution, illustrating the principles of both asymmetry in shape and distribution of encapsulated microparticles within the microfibers. Here, τ_1 represents the viscous shear force exerted to PDMS droplets near the microfiber surface, and τ_2 represents the viscous shear force to oil droplets far from the microfiber surface, with $\tau_1 > \tau_2$; (f and g) the length and width of PDMS microparticles, controlled by varying (f) the internal phase flow rate with a fixed external phase flow rate of 2 mL h^{-1} and (g) the external phase flow rate with a fixed internal phase flow rate of 0.1 mL h^{-1}.

eccentric placement of the inner tube within the outer tube ensured that the generated oil droplets were situated alongside the liquid jet (Movie S1, ESI†). Calcium chloride induced the crosslinking of sodium alginate, resulting in the formation of the hydrogel shell, and PDMS droplets were cured at 80 °C for two hours to produce the asymmetric microparticles.

Fig. 2b and c presents the wet microfibers immediately post-solidification. Notably, the encapsulated core microparticles exhibit both asymmetry in shape and an asymmetrical distribution within the microfibers. The asymmetric nature of these microfibers arises from the

solidification process, which progresses from the outer to the inner regions during alginate crosslinking. This gradient solidification induces a gradual decrease in liquid viscosity from the surface to the center of the forming microfiber. Consequently, an asymmetric shear force is generated, giving rise to the formation of asymmetric oil droplets, as illustrated in Fig. 2d and e. Control over the size of microfibers and the distribution and shape of internal microparticles can be achieved through the manipulation of liquid flow rates.

Fig. 2f illustrates variations in the shape and size of microparticles within the microfiber actuator by adjusting the internal phase flow rate while maintaining the external

© 2024 The Author(s). Co-published by the Institute of Process Engineering, Chinese Academy of Sciences and the Royal Society of Chemistry

Ind. Chem. Mater., 2024, **2**, 441–450 | **443**

phase flow rate at 2 mL h^{-1}. Increasing the inner phase flow rate results in an initial decrease in the length and width of the microparticles, followed by a stabilization of these dimensions. Fig. 2g demonstrates the modulation of microparticle size by altering the external phase flow rate, with a constant internal phase flow rate of 0.1 mL h^{-1}. Analogously, the microparticle size gradually diminishes and tends to flatten as the external phase flow rate increases. This underscores the highly controllable nature of microparticles within microfibers through the deliberate adjustment of flow rates.

2.3 Morphology of microfibers

Fig. 3 presents the morphological characteristics and surface structures of the manufactured asymmetric microfiber actuators. In Fig. 3a, scanning electron microscopy (SEM) images showcase the microfiber, with the microfiber shell wrapping PDMS microparticles to create a core–shell structure. Diatomite decorates the alginate surface, and all PDMS microparticles form individual knots interconnected by alginate–diatomite joints. The axis of the alginate–diatomite microfiber is intentionally off-centered from the axis of microparticles, resulting in the production of asymmetric microfiber actuators.

Fig. 3b provides a stereomicroscopy view of a microfiber actuator, characterized by a high level of asymmetry in both microparticles and the microfiber body. The tips of internal microparticles are not entirely covered by the alginate–diatomite shell, rendering them transparent. The markedly asymmetric microfiber actuator exhibits a flat backbone on one side and a ratchet-like structure on the other. Fig. 3c depicts the hydrated and dehydrated states of the microfibers. Relative to its dehydrated counterpart, the hydrating alginate–diatomite composite absorbs water, resulting in a larger volume. Due to the inherent asymmetry of the microfiber, the volume change distinctly varies between the flat backbone and the uneven ratchets, thereby driving the deformation of the microfiber. Notably, this volume change is reversible, occurring during both the hydration and dehydration processes of the microfiber actuators.

2.4 Reciprocal deformation

Fig. 4a visually depicts the deformation of an asymmetric microfiber actuator during the transition from a dehydrated to a hydrated state. The microfiber actuator initially undergoes bending and subsequently stretches (Movie S2, ESI†). In Fig. 4b, the temporal evolution of the radius of curvature is illustrated. Notably, the radius of curvature
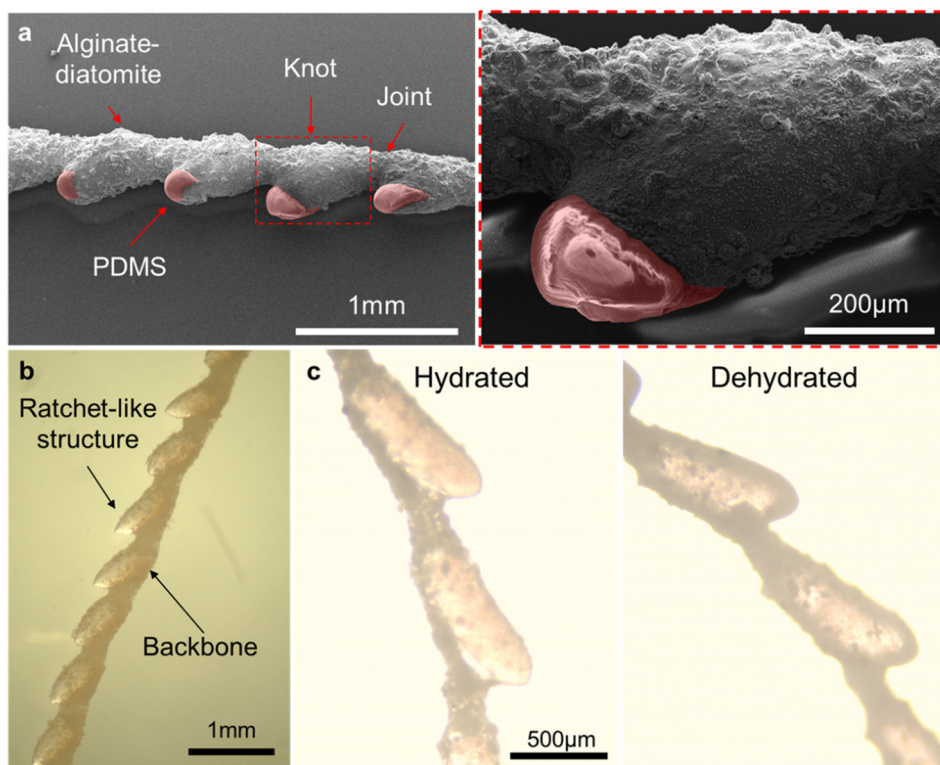

Fig. 3 Morphology of the asymmetric microfibers. (a) Scanning electron microscopy (SEM) images revealing the microstructure of the asymmetric microfiber. The magnified image (right) provides detailed insights into the structure and composition, showcasing the alginate–diatomite shell and partially exposed PDMS core. The red false colour indicates the bare PDMS protrusions; (b) OM illustrating the asymmetric morphology of the hydrated microfiber; (c) a comparison of microfiber morphologies under both hydrated (left) and dehydrated (right) states.
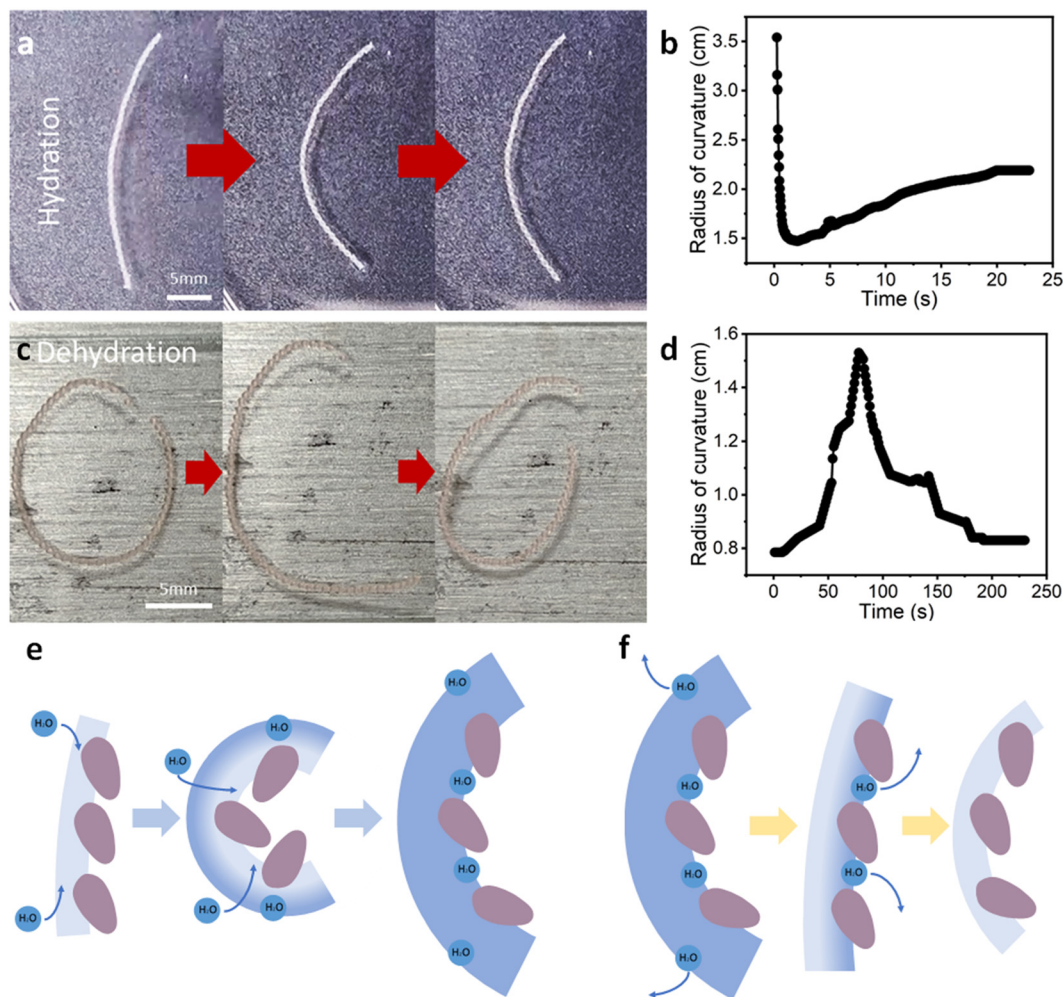
Fig. 4 The reciprocal deformation of asymmetric microfiber actuators. (a) Illustration of the deformation process of a microfiber actuator during hydration; (b) plot depicting the variation in the radius of curvature of the microfiber actuator during the hydration process over time; (c) demonstration of the deformation process of a microfiber actuator during dehydration; (d) the variation in the radius of curvature of the microfiber actuator during the dehydration process over time; (e and f) schematics outlining the mechanisms responsible for the deformation of microfibers during both (e) hydration and (f) dehydration processes, elucidating the key factors contributing to the observed reciprocal deformation of the microfiber actuators.

experiences an initial decrease, followed by an increase, and ultimately stabilizes over time, signifying a stable hydrated state. This characteristic decrease–increase in the radius of curvature is indicative of reciprocal deformation.

Fig. 4c showcases the deformation of an asymmetric microfiber actuator during the transition from a hydrated to a dehydrated state (Movie S3, ESI†). Placing the microfiber on a 50 °C plate accelerates the water evaporation and dehydration process. During dehydration, the microfiber first undergoes stretching and subsequently bending. The temporal variation of the radius of curvature during dehydration, as displayed in Fig. 4d, reveals an initial increase followed by a decrease until it reaches a constant value, confirming reciprocal deformation. Notably, this reciprocal deformation occurs during both the hydration and dehydration processes, in stark contrast to the unidirectional deformation characterized by a monotonic increase or decrease in curvature.

The distinct volume changes between the flat backbone and uneven ratchets, typically predictive of conventional unidirectional deformation, fail to explain the unique behaviour of reciprocal deformation observed in this study. We attribute this phenomenon to the anisotropy of the asymmetric microfiber actuator, which governs the absorption and desorption of water during hydration and dehydration, respectively.

Fig. 4e provides a schematic representation of how asymmetric microfiber actuators undergo reciprocal deformation during the hydration process. The hydrophilic nature of the alginate–diatomite shell and the hydrophobic properties of PDMS microparticles play a pivotal role. When the asymmetric microfiber actuator is put onto a water pool for hydration, the hydrophilic shell contacts water first, while hydrophobic microparticles are prevented from wetting. Consequently, the alginate–diatomite at the flat backbone side preferentially absorbs water more rapidly than the

© 2024 The Author(s). Co-published by the Institute of Process Engineering, Chinese Academy of Sciences and the Royal Society of Chemistry

Ind. Chem. Mater., 2024, **2**, 441–450 | **445**

alginate–diatomite near the PDMS ratchet side, leading to bending deformation toward the ratchet side and a decrease in the radius of curvature in the initial stage. The rapid saturation of water at the backbone side halts further absorption. However, the alginate–diatomite near the ratchet side continues to absorb water, causing an increase in volume and a subsequent force that stretches the microfiber against the initial bending, resulting in an increased radius of curvature in the second stage.

Reciprocal water regulation is also responsible for microfiber dehydration, as demonstrated in Fig. 4f. Placing the fully hydrated microfiber actuator on a hot plate accelerates dehydration. Given the larger volume of alginate–diatomite at the backbone side, water evaporates more rapidly, causing a larger and faster volume decrease and bending deformation toward the backbone side in the initial stage. The backbone side dries quickly and stops losing water upon complete dehydration, while the water loss process continues at the ratchet side. Consequently, in the second stage, the microfiber actuator experiences a more pronounced volume reduction at the ratchet side, inducing deformation in *a* direction opposite to that observed in the first stage. This elucidates the mechanism behind the two-stage variations in the radius of curvature observed in Fig. 4d.

The reciprocal deformation can be adjusted by modifying the morphology of microfiber actuators. In Fig. 5a, the microfiber actuators are depicted, fabricated by varying the liquid flow rate. As the internal flow rate increases, the size of internal microparticles enlarges while the spacing between microparticles decreases. Fig. 5b and c illustrates the evolution of the radius of curvature for the three microfiber actuators (shown in Fig. 5a) during the hydration and dehydration processes, respectively. By manipulating the morphology of microfiber actuators, both the curvature and magnitude of deformation in the initial and final states of the actuator are altered, while the overall trend of deformation remains consistent. During hydration (Fig. 5b), a two-stage reciprocal deformation is observed, identical to that in Fig. 4. Notably, during dehydration (Fig. 5c), a three-stage deformation is demonstrated, characterized by an initial decrease in the radius of curvature, followed by an increase, and ultimately another decrease. This three-stage deformation mode is attributed to the more intricate process of water loss during dehydration and suggests the potential for tuning the morphology of microfiber actuators to achieve more complex deformations.
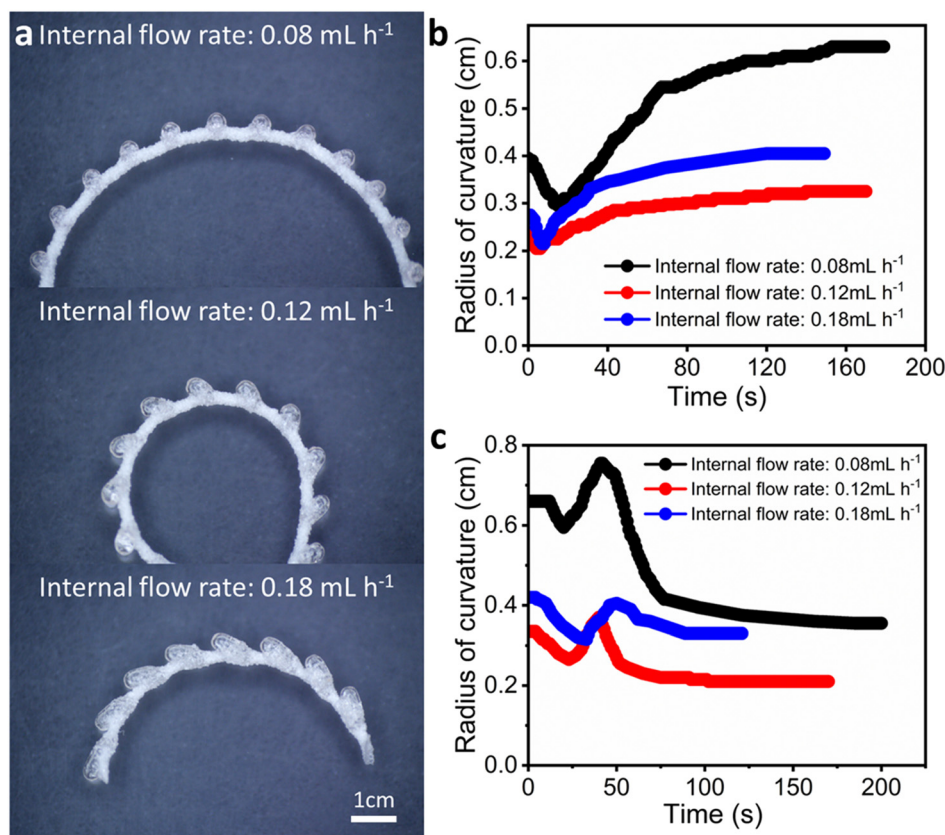

Fig. 5 Tunable reciprocal deformation of microfiber actuators. (a) Engineering the morphology of microfiber actuators by varying the internal flow rate with a constant external flow rate of 1.2 mL h^{-1}; (b and c) plots depicting variations in the radius of curvature of microfiber actuators during the (b) hydration and (c) dehydration processes over time.
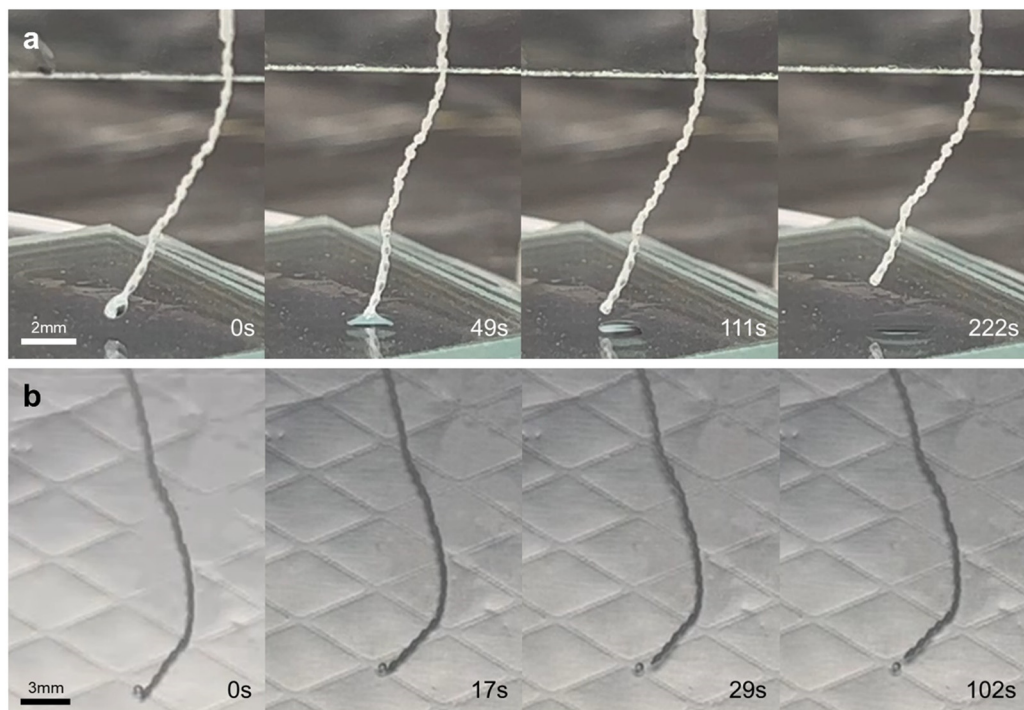
Fig. 6 Transportation of (a) a liquid droplet and (b) a solid particle by harnessing the reciprocal deformation of microfiber actuators.

2.5 Potential applications

Fig. 6 delineates potential applications of reciprocal-deformation microfiber actuators. The first proof-of-concept demonstration, illustrated in Fig. 6a, involves transporting droplets onto a substrate. In this scenario, one end of the microfiber actuator is anchored, while the other end remains free, carrying an oil droplet. The microfiber, initially in a hydrated state, is gradually dried, initiating the first-stage deformation that facilitates the controlled delivery of the oil droplet to the substrate. After droplet deposition, the microfiber actuator disengages from the substrate during the second-stage reciprocal deformation (Movie S4, ESI†).

The second demonstration, as depicted in Fig. 6b, focuses on transporting a solid cargo on a substrate. Here, the microfiber actuator has one end fixed and the other end free, close to a glass sphere. Analogously, the initially hydrated microfiber actuator undergoes a gradual drying process, leading to the first-stage deformation. This action propels the glass ball forward to the designated site. Following this task, the microfiber actuator autonomously disengages from the glass ball during the second-stage deformation (Movie S5, ESI†).

These demonstrations underscore the versatility of asymmetric microfiber actuators in manipulating both liquids and solids. This capability, in contrast to traditional actuators limited to unidirectional deformation, allows reciprocal-deformation microfiber actuators to maintain a certain distance from the target location after task execution. Such a unique capability opens avenues for a range of new applications, laying the groundwork for the development of next-generation actuators.

3 Conclusions

In summary, our study introduces a novel design of asymmetric microfiber actuators, distinguished by the unique feature of reciprocal deformation from traditional double-layer actuators. These microfiber actuators, constructed with a composite alginate–diatomite shell encapsulating hydrophobic PDMS microparticles, are precisely fabricated using droplet microfluidic technology, enabling controlled manipulation of morphology and internal microparticles. The identified anisotropy in the microfiber actuator, governing water absorption and desorption, proves instrumental in achieving reversible reciprocal deformation, shedding light on the complex interplay between the hydrophilic shell and hydrophobic microparticles. Furthermore, practical applications demonstrate the versatility of these actuators in manipulating both liquids and solids.

Future endeavors will concentrate on enhancing the overall performance of asymmetric microfiber actuators. Presently, the prototype actuators are hampered by limitations stemming from material selection and the slow water absorption/desorption process. These constraints manifest as long response times (on the order of minutes), relatively low actuation forces (ranging from 0.62 mN to 0.98 mN during hydration and 0.06 mN to 3.36 mN during dehydration), and reliability issues (stable for about ten cycles). These challenges can be effectively addressed through

© 2024 The Author(s). Co-published by the Institute of Process Engineering, Chinese Academy of Sciences and the Royal Society of Chemistry

Ind. Chem. Mater., 2024, **2**, 441–450 | **447**

various strategies, including accelerating the moisture absorption/desorption process, improving the mechanical strength of alginate, and introducing alternative energy sources for actuation such as thermal and wind energy. This study will not only advance the understanding of asymmetric microfiber actuators and their reciprocal deformation but also set the stage for the development of next-generation actuators, promising heightened versatility and functionality.

4 Experimental section

4.1 Fabrication of microfluidic device

The microfluidic device is comprised of two functional units: (i) a co-flow microchannel designed for generating oil-in-water (O/W) emulsions and (ii) a collection container facilitating the solidification of the microfiber shell. The co-flow microchannel was constructed by inserting an inner glass tube, ranging in diameter from 0.05 to 0.3 mm, into an outer glass tube with a diameter of 0.5 to 3 mm. The outlet of the outer tube was connected to a Petri dish serving as the collection container for the crosslinking of alginate, leading to the solidification of the microfiber shell.

4.2 Fabrication of microfibers

The O/W emulsions were initially generated in the microchannel to serve as liquid templates for the subsequent solidification of microfibers. The internal phase liquid consisted of a mixture of PDMS and silicone oil at a mass ratio of 1:1 to reduce the viscosity (376.3 mPa s), supplemented with a curing agent accounting for one-tenth of the total mass of PDMS and silicone oil. Simultaneously, the external phase liquid comprised an aqueous solution of sodium alginate (4 wt%) and diatomite (2 wt%), with a viscosity of 600.4 mPa s. Two syringe pumps were employed to precisely control the liquid flow rates. The produced emulsions were directed into a Petri dish containing an aqueous solution of calcium chloride (10 wt%), where the microfiber shell underwent solidification through the crosslinking of sodium alginate with calcium ions. After cross-linking, the wet microfibers were cured at 80 °C for two hours in a vacuum-dry oven. The microfiber actuators were finally obtained by drying the wet microfibers in the air for 30 minutes. The throughput of the microfiber actuators is about several meters per hour in experiments. Further enhancement in throughput can be achieved by increasing the flow rate, reducing the outlet microchannel diameter, and/or employing parallel microfluidic devices.

4.3 Microfiber actuation

The initiation of the hydration process involved immersing the dehydrated microfiber actuators in distilled water, prompting a reciprocal deformation in the curvature of the actuators. By contrast, the hydrated microfibers were carefully positioned on a heating plate set at 50 °C, facilitating the controlled evaporation of water to induce dehydration actuation. Notably, during this phase, the microfiber actuators underwent deformations opposite to those observed in the hydration process.

4.4 Characterization

Liquid viscosities were measured by a rotational viscometer (Shanghai Yixin, NDJ-1S). Microstructures of the asymmetric microfiber actuators were characterized by scanning electron microscopy (SEM, FEI Quanta FEG 450). The OMs were captured by a stereomicroscope (SOPTOP, SZM7054) equipped with a CCD camera (Harmony Technology HK Ltd., 20MSPM). Contact angles were measured by a contact angle goniometer (SINDIN, CSCIDC-350). Images were analyzed using ImageJ.

The actuation force was assessed using a semi-micro analytical balance (OHAUS, PX85). For the hydration actuation, one end of a dehydrated microfiber was secured on a glass substrate atop the semi-micro analytical balance, while the other end was affixed to a cantilever beam. The microfiber was then wetted with water, and changes in the balance reading were recorded. For the dehydration actuation, the above steps were repeated, replacing the dehydrated microfiber with a hydrated one, and changes in the balance reading during dehydration were recorded.

Author contributions

Conceptualization, P. Z.; methodology, P. Z. and S. W.; validation, P. Z., S. W. and Y. L.; formal analysis, Y. L.; investigation, Y. L.; resources, P. Z.; data curation, P. Z., S. W. and Y. L.; writing – original draft preparation, Y. L. and P. Z.; writing – review & editing, P. Z., S. W. and Y. L.; visualization, Y. L.; supervision, P. Z.; project administration, P. Z.; funding acquisition, P. Z.; Y. L. and S. W. share first authorship.

Conflicts of interest

A patent was filed based on the work in this study.

Acknowledgements

References

1　L. Hou, Z. Liang, X. Fan, J. Yu and F. Bao, Bioinspired self-coiling Janus microfiber actuators for micro-lifter and humidity sensing, *Sens. Actuators, B*, 2023, **394**, 134344.

2　C. Xin, Z. Ren, L. Zhang, L. Yang, D. Wang, Y. Hu, J. Li, J. Chu, L. Zhang and D. Wu, Light-triggered multi-joint microactuator fabricated by two-in-one femtosecond laser writing, *Nat. Commun.*, 2023, **14**, 4273.

3 X. Yang, L. Chang and N. O. Pérez-Arancibia, An 88-milligram insect-scale autonomous crawling robot driven by a catalytic artificial muscle, *Sci. Robot.*, 2020, **5**, eaba0015.

4 Y. Wang, T. Nitta, Y. Hiratsuka and K. Morishima, In situ integrated microrobots driven by artificial muscles built from biomolecular motors, *Sci. Robot.*, 2022, **7**, eaba8212.

5 A. Buguin, M.-H. Li, P. Silberzan, B. Ladoux and P. Keller, Micro-actuators: When artificial muscles made of nematic liquid crystal elastomers meet soft lithography, *J. Am. Chem. Soc.*, 2006, **128**, 1088–1089.

6 K. V. Selvan and M. S. Mohamed Ali, Micro-scale energy harvesting devices: Review of methodological performances in the last decade, *Renewable Sustainable Energy Rev.*, 2016, **54**, 1035–1047.

7 S. J. Park, S.-H. Park, S. Cho, D.-M. Kim, Y. Lee, S. Y. Ko, Y. Hong, H. E. Choy, J.-J. Min, J.-O. Park and S. Park, New paradigm for tumor theranostic methodology using bacteria-based microrobot, *Sci. Rep.*, 2013, **3**, 3394.

8 J. Li, B. Esteban-Fernández de Ávila, W. Gao, L. Zhang and J. Wang, Micro/nanorobots for biomedicine: Delivery, surgery, sensing, and detoxification, *Sci. Robot.*, 2017, **2**, eaam6431.

9 M. E. M. K. Abdelaziz, J. Zhao, B. Gil Rosa, H.-T. Lee, D. Simon, K. Vyas, B. Li, H. Koguna, Y. Li, A. A. Demircali, H. Uvet, G. Gencoglan, A. Akcay, M. Elriedy, J. Kinross, R. Dasgupta, Z. Takats, E. Yeatman, G.-Z. Yang and B. Temelkuran, Fiberbots: Robotic fibers for high-precision minimally invasive surgery, *Sci. Adv.*, 2024, **10**, eadj1984.

10 Y. Zheng, H. Zhao, Y. Cai, B. Jurado-Sánchez and R. Dong, Recent advances in one-dimensional micro/nanomotors: Fabrication, propulsion and application, *Nano-Micro Lett.*, 2022, **15**, 20.

11 T. Matsubara, J. S. Choi, D.-H. Kim and J.-W. Kim, A microfabricated pistonless syringe pump driven by electro-conjugate fluid with leakless on/off microvalves, *Small*, 2022, **18**, 2106221.

12 A. Barbot, M. Power, F. Seichepine and G.-Z. Yang, Liquid seal for compact micropiston actuation at the capillary tip, *Sci. Adv.*, 2020, **6**, eaba5660.

13 H. Lee, H. Kim, I. Ha, J. Jung, P. Won, H. Cho, J. Yeo, S. Hong, S. Han, J. Kwon, K. J. Cho and S. H. Ko, Directional shape morphing transparent walking soft robot, *Soft Rob.*, 2019, **6**, 760–767.

14 P. Won, K. K. Kim, H. Kim, J. J. Park, I. Ha, J. Shin, J. Jung, H. Cho, J. Kwon, H. Lee and S. H. Ko, Transparent soft actuators/sensors and camouflage skins for imperceptible soft robotics, *Adv. Mater.*, 2021, **33**, 2002397.

15 H. Kim, H. Lee, I. Ha, J. Jung, P. Won, H. Cho, J. Yeo, S. Hong, S. Han, J. Kwon, K.-J. Cho and S. H. Ko, Biomimetic color changing anisotropic soft actuators with integrated metal nanowire percolation network transparent heaters for soft robotics, *Adv. Funct. Mater.*, 2018, **28**, 1801847.

16 Y. Zhang, Y. Gong, B. Li, R.-M. Ma, Y. Che and J. Zhao, Light-driven continuous twist movements of microribbons, *Small*, 2019, **15**, 1804102.

17 S. Pevec and D. Donlagic, Resonant-opto-thermomechanical oscillator (ROTMO): A low-power, large displacement, high-frequency optically driven microactuator, *Small*, 2022, **18**, 2107552.

18 A. Belmonte, Y. Y. Ussembayev, T. Bus, I. Nys, K. Neyts and A. P. H. J. Schenning, Structural color actuators: Dual light and temperature responsive micrometer-sized structural color actuators, *Small*, 2020, **16**, 2070005.

19 X. Hui, J. Luo, R. Wang and H. Sun, Multiresponsive microactuator for ultrafast submillimeter robots, *ACS Nano*, 2023, **17**, 6589–6600.

20 H. Wang and B. Z. Tang, Efficient photo-actuator fabrication: Integrating microcrystal arrays with polymers, *Chem*, 2023, **9**, 3020–3022.

21 R. Yun, J. Che, Z. Liu, X. Yan and M. Qi, A novel electric stimulus-responsive micro-actuator for powerful biomimetic motions, *Nanoscale*, 2023, **15**, 12933–12943.

22 L. Chen, C. Liu, K. Liu, C. Meng, C. Hu, J. Wang and S. Fan, High-performance, low-voltage, and easy-operable bending actuator based on aligned carbon nanotube/polymer composites, *ACS Nano*, 2011, **5**, 1588–1593.

23 Y.-L. Zhang, J.-C. Li, H. Zhou, Y.-Q. Liu, D.-D. Han and H.-B. Sun, Electro-responsive actuators based on graphene, *Innovation*, 2021, **2**, 100168.

24 Y. Deng, A. Paskert, Z. Zhang, R. Wittkowski and D. Ahmed, An acoustically controlled helical microrobot, *Sci. Adv.*, 2023, **9**, eadh5260.

25 K. Han, C. W. Shields, N. M. Diwakar, B. Bharti, G. P. López and O. D. Velev, Sequence-encoded colloidal origami and microbot assemblies from patchy magnetic cubes, *Sci. Adv.*, 2017, **3**, e1701108.

26 S. M. Mirvakili, Q. P. Ngo and R. Langer, Polymer nanocomposite microactuators for on-demand chemical release via high-frequency magnetic field excitation, *Nano Lett.*, 2020, **20**, 4816–4822.

27 Y. Gao, B. Sprinkle, E. Springer, D. W. M. Marr and N. Wu, Rolling of soft microbots with tunable traction, *Sci. Adv.*, 2023, **9**, eadg0919.

28 R. L. Truby, Chemically fueling new microrobot abilities, *Science*, 2023, **381**, 1152–1153.

29 C. Zhou, P. Zhu, Y. Tian, M. Xu and L. Wang, Engineering micromotors with droplet microfluidics, *ACS Nano*, 2019, **13**, 6319–6329.

30 T. Zheng, P. P. S. S. Abadi, J. Seo, B.-H. Cha, B. Miccoli, Y.-C. Li, K. Park, S. Park, S.-J. Choi, R. Bayaniahangar, D. Zhang, S.-H. Lee, C.-K. Lee, A. Khademhosseini and S. R. Shin, Biocompatible carbon nanotube-based hybrid microfiber for implantable electrochemical actuator and flexible electronic applications, *ACS Appl. Mater. Interfaces*, 2019, **11**, 20615–20627.

31 P. Zhu, R. Chen, C. Zhou, M. Aizenberg, J. Aizenberg and L. Wang, Bioinspired soft microactuators, *Adv. Mater.*, 2021, **33**, 2008558.

32 T. H. Ware, M. E. McConney, J. J. Wie, V. P. Tondiglia and T. J. White, Voxelated liquid crystal elastomers, *Science*, 2015, **347**, 982–984.

© 2024 The Author(s). Co-published by the Institute of Process Engineering, Chinese Academy of Sciences and the Royal Society of Chemistry

Ind. Chem. Mater., 2024, **2**, 441–450 | **449**

33 Q. He, Z. Wang, Y. Wang, Z. Wang, C. Li, R. Annapooranan, J. Zeng, R. Chen and S. Cai, Electrospun liquid crystal elastomer microfiber actuator, *Sci. Robot.*, 2021, **6**, eabi9704.

34 W. Hou, J. Wang and J.-A. Lv, Bioinspired liquid crystalline spinning enables scalable fabrication of high-performing fibrous artificial muscles, *Adv. Mater.*, 2023, **35**, 2211800.

35 D. T. Tran, A. S. Yadav, N.-K. Nguyen, P. Singha, C. H. Ooi and N.-T. Nguyen, Biodegradable polymers for micro elastofluidics, *Small*, 2023, 2303435.

36 L. Cecchini, S. Mariani, M. Ronzan, A. Mondini, N. M. Pugno and B. Mazzolai, 4D printing of humidity-driven seed inspired soft robots, *Adv. Sci.*, 2023, **10**, 2205146.

37 P. Zhu, R. Chen, C. Zhou, Y. Tian and L. Wang, Asymmetric fibers for efficient fog harvesting, *Chem. Eng. J.*, 2021, **415**, 128944.

38 P. Zhu and L. Wang, Microfluidics-enabled soft manufacture of materials with tailorable wettability, *Chem. Rev.*, 2022, **122**, 7010–7060.